

# A Scheme to Numerically Evolve Data for the Conformal Einstein Equation

Peter Hübner

(pth@aei-potsdam.mpg.de)

Max-Planck-Institut für Gravitationsphysik  
Albert-Einstein-Institut  
Schlaatzweg 1  
D-14473 Potsdam  
FRG

short title: Integrating the Conformal Einstein Equation

PACS numbers: 0420G, 0420H, 0430

This is the second paper in a series describing a numerical implementation of the conformal Einstein equation. This paper deals with the technical details of the numerical code used to perform numerical time evolutions from a “minimal” set of data.

We outline the numerical construction of a complete set of data for our equations from a minimal set of data. The second and the fourth order discretisations, which are used for the construction of the complete data set and for the numerical integration of the time evolution equations, are described and their efficiencies are compared. By using the fourth order scheme we reduce our computer resource requirements — with respect to memory as well as computation time — by at least two orders of magnitude as compared to the second order scheme.

## I. INTRODUCTION

We calculate solutions to the Einstein equation arising from hyperboloidal initial data by solving the conformal field equation. In the first paper in this series [1] the ideas behind the conformal approach, their mathematical foundation, and the benefits of it have been discussed in detail. In this paper we discuss the numerical details of the part of the implementation which calculates the time evolution from a minimal set of data consisting of the conformal 3-metric  $h_{ab}$  and the conformal extrinsic curvature  $k_{ab}$  as well as the conformal factor  $\Omega$  and its time derivative  $\Omega_0$ . The latter relate  $(h_{ab}, k_{ab})$  to the physical data.

To be able to test the numerics described here, we take known exact solutions given in terms of the conformal metric  $g_{ab}$  and the conformal factor  $\Omega$ , perform numerical coordinate transformations to hide obvious symmetries, and calculate in a straightforward way a minimal set of data from the transformed solution. Then we extend the minimal set of data to a complete set of conformal data. The calculation of the complete data set is a delicate numerical issue. In section II we discuss why it is so and we show how to solve this problem. After having calculated a complete set of data we can start the actual time integration. In section III we describe in detail the second and the fourth order scheme used to numerically integrate the symmetric hyperbolic time evolution equations.

In the section IV we outline properties of the exact solutions important for the tests, the tests themselves, and the results of the comparisons between the two schemes.

In the tests based on conformal Minkowski data we reconstruct the whole future of the initial slice as well as null infinity and even timelike infinity after a finite number of time steps. Obviously we can then stop the calculation. As suggested by the theorems in [2] we can expect to cover the future of the initial slice in all cases of sufficiently small asymptotically Minkowskian data, i. e. for all gravitational wave data not forming singularities or black holes, by one finite grid.

In the other tests we use asymptotically A3 solutions (cf. subsection IV A). These are solutions which in general contain gravitational radiation but are special in the sense that they possess a conformal structure which becomes singular towards timelike infinity. We compare the numerical result with the analytic solution after covering a certain integration time. To check stability we have also performed much larger numbers of time steps and we did not encounter any numerical problems, but the numerical evolution slows down for the following reason. In the given coordinates, the light cones in the interior become flatter and flatter the closer they are to the singular timelike infinity. Therefore, the Courant-Friedrichs-Levy condition must enforce smaller and smaller time steps and it prevents us from reaching timelike infinity in the numerical integration, unless we embark upon a more detailed study (which is beyond the goal of this paper).

Comparing the second order with the fourth order scheme we found the fourth order scheme surpassing the second order scheme in three dimensional calculations by an at least two orders of magnitude more efficient use of computer resources. In all cases we tested the combination of the fourth order scheme with grids with 100 gridpoints in each space dimensions was sufficient to achieve relative errors of less than one percent. The resulting moderate memory and computer time requirements allow us to do our calculations, including the ones with three space dimensions, on medium size parallel computers which are nowadays available in many physics institutes with numerical orientation.

In appendix A we give a short review of the computational science aspects of the code.

## II. CONSTRUCTING A COMPLETE DATA SET

To avoid too many repetitions, we assume the reader to be familiar with the general approach as well as with the equations discussed in part one of this series, and we shall refer to equation (n) of part one by writing (I/n).

### A. Minimal set of data from exact solutions

The known solutions of the conformal field equations have all high degrees of symmetries, and usually the metric  $g_{a'b'}$  and the rescaling factor  $\Omega$  are written in terms of symmetry adapted coordinates  $x_s^{a'} = (t_s, x_s, y_s, z_s)$ . In these coordinates many variables and major parts of the equations are identically zero, hence they are of limited use for testing. Things become more interesting if we make coordinate transformations which hide the symmetries. For technical reason we prescribe the inverse of the coordinate transformation,

$$x_s^{a'} = x_s^{a'}(x^a). \quad (1)$$

Then the components of the metric  $g_{ab}$  in the new coordinates  $g_{ab}$  are

$$g_{ab}(x^a) = g_{a'b'}(x_s^{a'}(x^a))(\partial_a x_s^{a'})(\partial_b x_s^{b'}). \quad (2)$$

The derivatives are numerically calculated by evaluating fourth order stencils according to (10a) with respect to an imaginary grid with one tenth of the grid spacing of the real grid. From equation (2) we can read off the first elements of a minimal set of data on the hypersurface defined by  $t = t_0$ , namely the components of the 3-metric  $h_{ab}$ , as the  $\{x, y, z\}$ -components of  $g_{ab}$ . The next element of a minimal set, the scalar  $\Omega$ , only changes its functional form under the coordinate transformation,  $\Omega(x^a) = \Omega(x_s^{a'}(x^a))$ .

After numerically calculating time and space derivatives of  $(h_{ab}, \Omega)$ , equation (I/13a) respectively (I/13h) are used to calculate the missing elements  $(k_{ab}, \Omega_0)$  of a minimal set of data. The needed lapse  $N$  and shift  $N^a$  are obtained as the solution of the system of equations  $g_{tt} = -N^2 + h_{ab}N^aN^b$  and  $g_{\{x,y,z\}t} = h_{\{x,y,z\}b}N^b$ .

During the time evolution we have to prescribe the gauge source functions  $q = \ln(N/\sqrt{h})$ , shift  $N^a$ , and Ricci scalar  $R$ . The function  $q = \ln(N/\sqrt{h})$  and the shift  $N^a$  are calculated from the coefficients of  $g_{ab}$  on each slice in analogy to the approach on the initial slice, the Ricci scalar  $R$  is given as function of the coordinates.

## B. From a minimal to a complete set of conformal data

To calculate the remaining initial data  $(\gamma^a_{bc}, {}^{(0,1)}\hat{R}_a, {}^{(1,1)}\hat{R}_{ab}, E_{ab}, B_{ab}, \Omega_a, \omega)$  from the minimal set we use certain combinations of the conformal constraints (I/14). In particular, we use

$$\mathcal{N}_{\mathbf{h}abc} = 0, \quad (3a)$$

$$\mathcal{N}_{\mathbf{k}ab}{}^b = 0, \quad (3b)$$

$$\mathcal{N}_{\gamma ab}{}^{ab} = 0, \quad (3c)$$

$$\mathcal{N}_{\Omega a} = 0, \quad (3d)$$

$$\mathcal{N}_{\Omega_a}{}^a = 0, \quad (3e)$$

$$\mathcal{N}_{\Omega_a ab} = 0, \quad (3f)$$

$${}^{(3)}\epsilon_a{}^{cd}\mathcal{N}_{\mathbf{k}cdb} = 0, \quad (3g)$$

to solve for  $\gamma^a_{bc}, {}^{(0,1)}\hat{R}_a, {}^{(1,1)}\hat{R}_a{}^a, \Omega_a, \omega, f_{(1,1)\hat{R}ab} := \Omega {}^{(1,1)}\hat{R}_{ab}, f_{Bab} := \Omega B_{ab}$  respectively.

To extract  ${}^{(1,1)}\hat{R}_{ab}$  and  $B_{ab}$  from  $f_{(1,1)\hat{R}ab}$  and  $f_{Bab}$  we have to divide by  $\Omega$ . This division by  $\Omega$  is numerically the most delicate part of the construction of a complete set of data. It will be described in the next subsection. After the division we use  ${}^{(1,1)}\hat{R}_{ab}$  to calculate  $f_{Eab} := \Omega E_{ab}$  from

$$\mathcal{N}_{\gamma acb}{}^c = 0. \quad (3h)$$

To determine  $E_{ab}$  from  $f_{Eab}$  we again have to divide by  $\Omega$ .

### C. Dividing by $\Omega$

In [3] the smoothness of the limits  $\lim_{\Omega \rightarrow 0} \frac{f}{\Omega}$  has been analysed in detail. In a straightforward implementation of the approach used there we would divide by  $\Omega$  outside the set  $\mathcal{S}$  on the initial slice and use l'Hopital's rule at  $\mathcal{S}$ , where  $\Omega$  vanishes. Then a picture like the one shown in figure 1 would result.

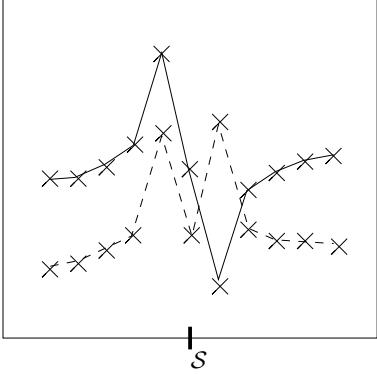


FIG. 1. Sketch of  ${}^{(1,1)}\hat{R}_{ab}$  (solid line) and  $E_{ab}$  (dashed line) near  $\mathcal{S}$  as obtained by a combination of a division by  $\Omega$  outside  $\mathcal{S}$  and the application of l'Hopital's rule at  $\mathcal{S}$ . The crosses denote gridpoints.

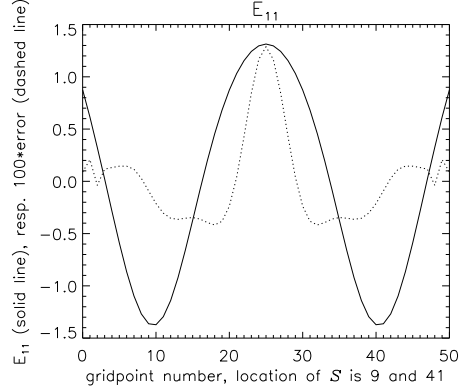


FIG. 2. Result of our method applied to an A3 spacetime on a  $50^3$  grid. The solid line shows  $E_{11} + 2.5$  along a typical  $(y, z) = \text{const}$  line, which intersects  $\mathcal{S}$  at gridpoints 9 and 41. The dashed line shows  $100 \times$  the difference to an  $100^3$  calculation. Its non-smoothness near the boundary is caused by changing from a symmetric to an asymmetric stencil. It does not affect the boundary treatment described in subsection III C.

The reason for the pole like structure near  $\mathcal{S}$  is simple, as we will immediately see. Let us assume, for simplicity, that we have one space dimension only, that  $\Omega = 0$  at  $x = 0$ , and that the corresponding gridpoint has number 0. In the process of calculating  $(f_{(1,1)\hat{R}}, f_B, f_E)$  numerical derivatives are taken, therefore each  $f$  deviates from the exact value  $f_e$  by a discretisation error,  $f = f_e + a_f(\Delta x)^n$ , where  $n$  is the order of the scheme. We now make a Taylor expansion of  $f_e$  and  $\Omega$  around  $x = 0 + dx$  and recognise that we lost near point 0 one order of accuracy, since  $\frac{f}{\Omega} = \frac{f_e}{\Omega} + \frac{a_f}{d_x \Omega|_0} \frac{\Delta x}{dx} (\Delta x)^{n-1}$  and  $\frac{\Delta x}{dx}$  is always of order 1 at the neighbours of gridpoint 0.  $\frac{\Delta x}{dx}$  changes sign at point 0, hence the form of the solid line in figure 1. When dividing by  $\Omega$  a second time to calculate  $E_{ab}$  we see by the same kind of argument and by recalling, that the pole like structure of the solid line enters into  $f_{E_{ab}}$ , that we get the dashed line in figure 1.

This non-smoothness of the discretisation error and the loss of two orders of accuracy in the initial data is unacceptable mainly for two reasons. Firstly, discretisation schemes for symmetric hyperbolic equations tend to react to these kinds of non-smoothness in the initial data with significant drops in the convergence order. Secondly, this defect would be most significant in the neighbourhood of  $\mathcal{S}$  and would hence establish a kind of boundary at  $\mathcal{S}$  which would eliminate many advantages of the conformal method.

We tried various methods to remove the pole-like structure by some kind of smoothing

procedure. Although the behaviour could be improved, the phenomena never disappeared completely. The problematic behaviour could almost be cured by first subtracting a function with values of the order of the discretisation error from  $f$  on the whole grid, making  $f$  exactly vanish at  $\mathcal{S}$ , and then dividing by  $\Omega$ .<sup>1</sup> We did not pursue this approach beyond the asymptotically A3 scenarios because we did not see how to generalise it to arbitrary  $\mathcal{S}$  and in particular because we found the following approach which works for arbitrary  $\mathcal{S}$ . Instead of solving the equation  $g\Omega = f$  for  $g$ , we determine  $g$  as solution to an elliptic equation of the type

$${}^{(3)}\Delta(\Omega^2 g - \Omega f) = 0, \quad (4)$$

where the symbol  ${}^{(3)}\Delta$  denotes the Laplace operator of  ${}^{(3)}\nabla_a$ , that is  ${}^{(3)}\Delta := {}^{(3)}\nabla^a {}^{(3)}\nabla_a$ . If we write this as an equation for  $u := \Omega^2 g - \Omega f$ , we see that the uniquely determined solution for the boundary values  $u|_{\text{boundary}} = 0$  is  $u = 0$ , i. e.  $g = f/\Omega$ .

Written as equation for  $g$  equation (4) reads

$$\Omega^2 {}^{(3)}\Delta g + 4\Omega ({}^{(3)}\nabla^a \Omega) ({}^{(3)}\nabla_a g) + [2 ({}^{(3)}\nabla^a \Omega) ({}^{(3)}\nabla_a \Omega) + 2\Omega {}^{(3)}\Delta \Omega] g = f {}^{(3)}\Delta \Omega + 2 ({}^{(3)}\nabla^a \Omega) ({}^{(3)}\nabla_a f) + \Omega {}^{(3)}\Delta f. \quad (5)$$

If the derivatives are discretised by symmetric stencils like (9) or (10), the  $({}^{(3)}\nabla_a g)$  term has a sign which is known to cause a tendency for instabilities [5]. To avoid the resulting numerical problems we add

$$- \eta ({}^{(3)}\nabla^a \Omega) ({}^{(3)}\nabla_a (\Omega g - f)) = 0 \quad (6)$$

to equation (5) and obtain

$$\Omega^2 {}^{(3)}\Delta g + (4 - \eta)\Omega ({}^{(3)}\nabla^a \Omega) ({}^{(3)}\nabla_a g) + [(2 - \eta) ({}^{(3)}\nabla^a \Omega) ({}^{(3)}\nabla_a \Omega) + 2\Omega {}^{(3)}\Delta \Omega] g = f {}^{(3)}\Delta \Omega + (2 - \eta) ({}^{(3)}\nabla^a \Omega) ({}^{(3)}\nabla_a f) + \Omega {}^{(3)}\Delta f. \quad (7)$$

This is the linear elliptic equation we solve after we have numerically calculated the function  $f$ , which is due to discretisation errors not exactly 0 at  $\mathcal{S}$ . Instead of having to divide by  $\Omega$  on the whole grid we only have to divide by  $\Omega$  on the true<sup>2</sup> grid boundaries to provide boundary values for our elliptic equation. This does not constitute any numerical problem, since  $\Omega$  is significantly different from 0 at the true grid boundaries.

Equation (7) tells us that on  $\mathcal{S}$

$$g = \frac{f {}^{(3)}\Delta \Omega}{(2 - \eta) ({}^{(3)}\nabla^a \Omega) ({}^{(3)}\nabla_a \Omega)} + \frac{({}^{(3)}\nabla^a \Omega) ({}^{(3)}\nabla_a f)}{({}^{(3)}\nabla^a \Omega) ({}^{(3)}\nabla_a \Omega)}, \quad (8)$$

which is a correct answer, since  $f$  vanishes up to the discretisation error. Since  ${}^{(3)}\nabla_a \Omega|_{\mathcal{S}} \neq 0$  in any extended hyperboloidal initial value problem, expression (8) is well-defined.

---

<sup>1</sup>Jörg Frauendiener has developed a sophisticated way to combine this kind of idea with spectral decomposition in his 2D code for asymptotically A3 spacetimes [4].

<sup>2</sup>For a definition of “true” in the context of boundaries see subsection III C.

Of course the properties of equation (7) depend on the parameter  $\eta$ : For  $\eta = 0$  it is difficult to get a stable numerical scheme, for  $\eta = 2$  there is no solution possible if  $f|_S \neq 0$ , for  $\eta = 3$  the discretised system can be written as symmetric matrix [6, equation(5.1.18)], for  $\eta = 4$  the term  $({}^3\nabla_a g)$  has vanishing coefficient, and for  $\eta = 8$  the system possesses the same principal part as the Yamabe equation, which will play a crucial role in the next part of the series, where we describe how to generate minimal sets of data not representing known exact solutions. At least the later three choices for  $\eta$  deliver values of  $g$  which converge to the exact  $g$  with a smooth discretisation error and without loss of one order of convergence. Figure 2 shows the smoothness and the error for a run with a pretty coarse grid.

The default choice in the code is  $\eta = 8$ , together with  $\delta_{ab}$  as 3-metric. To exclude the possibility of having calculated a spurious solution of equation (7), except for the  $\eta = 0$  case we have not shown uniqueness, we evaluate the constraints (I/14) to check consistency.

To discretise we substitute

$$\partial_x f \rightarrow \frac{1}{2\Delta x} (f_{i+1,j,k} - f_{i-1,j,k}), \quad (9a)$$

$$\partial_x^2 f \rightarrow \frac{1}{(\Delta x)^2} (f_{i,j,k} - 2f_{i,j,k} + f_{i-1,j,k}), \quad (9b)$$

and their equivalents for the  $y$  and  $z$  coordinates to obtain second order approximations, respectively

$$\partial_x f \rightarrow \frac{1}{12\Delta x} (-f_{i+2,j,k} + 8f_{i+1,j,k} - 8f_{i-1,j,k} + f_{i-2,j,k}), \quad (10a)$$

$$\partial_x^2 f \rightarrow \frac{1}{12(\Delta x)^2} (-f_{i+2,j,k} + 16f_{i+1,j,k} - 30f_{i,j,k} + 16f_{i-1,j,k} - f_{i-2,j,k}), \quad (10b)$$

and their equivalents for the  $y$  and  $z$  coordinates to obtain fourth order approximations.

The elliptic equation (7) then becomes a set of linear equations for the values  $g_{i,j,k}$  of  $g$  at gridpoints  $(i, j, k)$ , denoted by the vector  $\underline{u}$ :

$$\underline{\underline{C}} \underline{u} = \underline{r}, \quad (11)$$

with some sparse matrix  $\underline{\underline{C}}$  depending on the stencils. The vector  $\underline{r}$  is given by the prescribed boundary values and the right hand side of equation (7). The matrix  $\underline{\underline{C}}$  would become singular if  $\Omega$  and  $\partial_a \Omega$  vanished simultaneously at one gridpoint. For an extended hyperboloidal initial value problem this cannot happen.

Equation (11) is solved iteratively by using the algebraic multigrid library (AMG) by K. Stüben from the Gesellschaft für Mathematik und Datenverarbeitung. AMG analyses the algebraic structure of the matrix  $\underline{\underline{C}}$  and derives from the structure a strategy to apply multigrid techniques to accelerate the convergence rate of the iterative solution of equation (11). Since the structure analysis happens automatically in AMG, it is very easy to program elliptic solvers for different stencils or for grids with different topologies, one only needs to change the computation of  $\underline{\underline{C}}$  and  $\underline{r}$ , but not the multigrid part. This convenience more than outweighs the computational overhead from analysing the algebraic structure of  $\underline{\underline{C}}$  once in each program run. The interested reader can find a detailed description of AMG in [7,8].

Before we end this section, we should make a remark about the accuracy which we can achieve. Increasing the number of gridpoints decreases the discretisation error. On the

other side, it is well-known that matrix inversion, here solving equation (11), amplifies rounding errors. The amplification grows with the size of the matrix  $\underline{\underline{C}}$ , which is determined by the number of gridpoints. Due to the amplification of the rounding errors refinement of the grid beyond a certain threshold will not improve the accuracy of the solution. When we surpass the  $500^2$  grid size in a fourth order scheme calculation, rounding errors become a visible contribution to the total error. The size of the relative error in the solutions of the elliptic solver is then of order  $10^{-11}$ . A remnant of that lower bound to the convergence of the scheme becomes visible in the curve for the  $640^2$  grid size in figure 8.

### III. THE DISCRETISATION OF THE TIME INTEGRATOR

In this section, where we describe the discretisation of the time evolution equations (I/13), we write our equations formally as

$$\partial_t \underline{f} + \underline{\underline{A}}^i(\underline{f}) \partial_i \underline{f} = \underline{b}(\underline{f}). \quad (12)$$

Our system of equation is, up to some simple algebraic manipulations, a quasilinear symmetric hyperbolic system of first order. One of the characteristic properties of these kinds of systems is the existence of a maximal set of real characteristics and thus of a finite propagation speed of signals. In implicit schemes the numerical speed of propagation is infinite, or at least very large. To mimic the finiteness of the propagation speed we therefore have to use explicit schemes. Moreover, we have to expect that parts of our slices run into singularities during time evolution. Due to the infinite numerical propagation speed in implicit schemes, the occurrence of a single gridpoint with singular values of a single variable would cease the calculation. In explicit schemes we can in principle continue the calculation to cover at least part of the remaining spacetime [9,10]. For these reasons we have only evaluated explicit schemes.

#### A. The second order scheme

##### 1. General considerations for the choice of the scheme

The general form of explicit second order schemes in  $1D^3$  is given by the so-called  $S_\beta^\alpha$  schemes [11], which contain the widely used MacCormack and Lax-Wendroff schemes. Their extension to 2D and 3D is not unique and most of the schemes obtained distinguish certain propagation directions. For many of the schemes with a distinguished direction, e. g. all generalisations of the MacCormack scheme, the occurrence of a weak instability could be shown already for the advection equation, if the propagation direction is opposite to the distinguished direction [12]. This instability is of a strange character and hard to detect [12,13]. Since for quasilinear equations the propagation directions depend on the data and may change during the time evolution, those schemes, even if initially stable, may become unstable.

---

<sup>3</sup>We call a calculation nD, if it uses an n-dimensional space grid.

To avoid distinguishing certain directions and dealing with these instabilities we implemented the rotated Richtmyer scheme, the extension of Lax-Wendroff which does not distinguish propagation directions. For our evolution equations combined with strong data even the rotated Richtmyer scheme turned out to be unstable. A grid mode with a wave length of ten gridpoints was not damped sufficiently. Although we could make this grid mode vanish by adding artificial viscosity, the scheme was still not stable, a 20 gridpoint grid mode appeared later in the time evolution. In the linearised equations the growth rate of the instability was significantly weaker, the linearised equations without source were stable, as predicted by the theory. To be able to treat the principle part, which determines the propagation directions, by rotated Richtmyer and the sources by something else, we use Strang splitting.

## 2. The implemented second order scheme

In the Strang splitting ansatz one formally writes equation (12) as an equation for the principal part,

$$\partial_t \underline{f} + \underline{A}^i(f) \partial_i \underline{f} = 0, \quad (13)$$

and an equation for the sources,

$$\partial_t \underline{f} = \underline{b}(f). \quad (14)$$

To integrate equation (13) we use the rotated Richtmyer scheme: First, we calculate a half grid,

$$\begin{aligned} \underline{f}_{i+1/2,j+1/2,k+1/2}^l = \frac{1}{2^3} & \left( \underline{f}_{i,j,k}^l + \underline{f}_{i+1/2,j,k}^l + \underline{f}_{i,j+1/2,k}^l + \underline{f}_{i+1/2,j+1/2,k}^l \right. \\ & \left. + \underline{f}_{i,j,k+1/2}^l + \underline{f}_{i+1/2,j,k+1/2}^l + \underline{f}_{i,j+1/2,k+1/2}^l + \underline{f}_{i+1/2,j+1/2,k+1/2}^l \right), \end{aligned}$$

and the derivatives thereon,

$$\begin{aligned} \partial_x \underline{f}_{i+1/2,j+1/2,k+1/2}^l = \frac{1}{2^{3-1} \Delta x} & \left( -\underline{f}_{i,j,k}^l + \underline{f}_{i+1,j,k}^l - \underline{f}_{i,j+1,k}^l + \underline{f}_{i+1,j+1,k}^l \right. \\ & \left. - \underline{f}_{i,j,k+1}^l + \underline{f}_{i+1,j,k+1}^l - \underline{f}_{i,j+1,k+1}^l + \underline{f}_{i+1,j+1,k+1}^l \right), \end{aligned}$$

$$\partial_y \underline{f}_{i+1/2,j+1/2,k+1/2}^l \text{ and } \partial_z \underline{f}_{i+1/2,j+1/2,k+1/2}^l \text{ in analogy,}$$

to take the predictor step:

$$\underline{f}_{\mathcal{P}^{i+1/2,j+1/2,k+1/2}}^{l+1/2} = \underline{f}_{i+1/2,j+1/2,k+1/2}^l - \frac{\Delta t}{2} \underline{A}^m(\underline{f}_{i+1/2,j+1/2,k+1/2}^l) \partial_m \underline{f}_{i+1/2,j+1/2,k+1/2}^l.$$

Then, we average again,

$$\begin{aligned} \underline{f}_{\mathcal{P}^{i,j,k}}^{l+1/2} = \frac{1}{2^3} & \left( \underline{f}_{\mathcal{P}^{i-1/2,j-1/2,k-1/2}}^l + \underline{f}_{\mathcal{P}^{i+1/2,j-1/2,k-1/2}}^l + \underline{f}_{\mathcal{P}^{i-1/2,j+1/2,k-1/2}}^l \right. \\ & + \underline{f}_{\mathcal{P}^{i+1/2,j+1/2,k-1/2}}^l + \underline{f}_{\mathcal{P}^{i-1/2,j-1/2,k+1/2}}^l + \underline{f}_{\mathcal{P}^{i+1/2,j-1/2,k+1/2}}^l \\ & \left. + \underline{f}_{\mathcal{P}^{i-1/2,j+1/2,k+1/2}}^l + \underline{f}_{\mathcal{P}^{i+1/2,j+1/2,k+1/2}}^l \right), \end{aligned}$$

and again calculate the derivatives,



$$\partial_x \underline{f}_{\mathcal{P}^{i,j,k}}^{l+1/2} = \frac{1}{2^{3-1}\Delta x} \left( -\underline{f}_{\mathcal{P}^{i-1/2,j-1/2,k-1/2}}^l + \underline{f}_{\mathcal{P}^{i+1/2,j-1/2,k-1/2}}^l \right. \\
\left. -\underline{f}_{\mathcal{P}^{i-1/2,j+1/2,k-1/2}}^l + \underline{f}_{\mathcal{P}^{i+1/2,j+1/2,k-1/2}}^l \right. \\
\left. -\underline{f}_{\mathcal{P}^{i-1/2,j-1/2,k+1/2}}^l + \underline{f}_{\mathcal{P}^{i+1/2,j-1/2,k+1/2}}^l \right. \\
\left. -\underline{f}_{\mathcal{P}^{i-1/2,j+1/2,k+1/2}}^l + \underline{f}_{\mathcal{P}^{i+1/2,j+1/2,k+1/2}}^l \right), \\
\partial_y \underline{f}_{i,j,k}^{l+1/2} \text{ and } \partial_z \underline{f}_{i,j,k}^{l+1/2} \text{ in analogy,}$$

to take the corrector step:

$$\underline{f}_{\mathcal{P}^{i,j,k}}^{l+1} = \mathcal{P} \underline{f}_{i,j,k}^l := \underline{f}_{i,j,k}^l - \Delta t \underline{A}^m(\underline{f}_{\mathcal{P}^{i,j,k}}^{l+1/2}) \partial_m \underline{f}_{\mathcal{P}^{i,j,k}}^{l+1/2}. \quad (15)$$

To integrate the source equation (14) we use the pseudo-implicit Heun scheme [14], since it is said to be similarly robust in the case of stiff equations as implicit schemes:

$$\underline{f}_{\mathcal{S}^{i,j,k}}^{l+1/n} = \underline{f}_{\mathcal{S}^{i,j,k}}^l + \Delta t \underline{b}(\underline{f}_{i,j,k}^l) \\
\underline{f}_{\mathcal{S}^{i,j,k}}^{l+m/n} = \underline{f}_{\mathcal{S}^{i,j,k}}^l + \frac{\Delta t}{2} \left( \underline{b}(\underline{f}_{\mathcal{S}^{i,j,k}}^l) + \underline{b}(\underline{f}_{\mathcal{S}^{i,j,k}}^{l+(m-1)/n}) \right), \quad 2 \leq m \leq n.$$

Here  $n$  is the number of iterations.

$$\underline{f}_{\mathcal{S}^{i,j,k}}^{l+1} =: \mathcal{S} \underline{f}_{\mathcal{S}^{i,j,k}}^l \quad (16)$$

There are two standard ways to combine the integration operator  $\mathcal{P}$  for the principal part with the integration operator  $\mathcal{S}$  for the source terms, the Strang I and the Strang II scheme [15]. They have the disadvantage of consuming additional memory and requiring many loops over the grids. By using different schemes for the odd and even time steps, namely

$$\underline{f}_{i,j,k}^{l+2n-1} = \mathcal{S} \mathcal{P} \underline{f}_{i,j,k}^{l+2n-2}$$

and

$$\underline{f}_{i,j,k}^{l+2n} = \mathcal{P} \mathcal{S} \underline{f}_{i,j,k}^{l+2n-1}, \quad (17)$$

we avoid these disadvantages and obtain a scheme which is globally second order, although the coefficient of the leading term in the discretisation error jumps between odd and even steps.

In the numerical implementation we use three grids to store the variables, the gauge source functions, and the intermediate values. Even if we calculated the gauge source functions by some global second order procedure, which were of course incompatible with hyperbolicity of the system, our scheme would be second order.

## B. The fourth order scheme

In the 3D test calculations it turned out that to obtain the accuracy which we regard as necessary would require more computer resources than available to us. We therefore, and

due to the strong recommendations by H.-O. Kreiss, tried the “method of line” to build higher order schemes. Since the first results on 3D calculations on the Maxwell equations and the SU(2)-Yang-Mills equations confirmed the statement, that the required number of gridpoints per coordinate directions is reduced by a factor of five [16], we combined the method of line with the conformal approach.

In the method of line we formally write

$$\partial_t \underline{f} = \underline{B}(\underline{f}, \partial_i \underline{f}), \quad (18)$$

where  $\underline{B}(\underline{f}, \partial_i \underline{f}) = -\underline{A}^i(\underline{f}) \partial_i \underline{f} + \underline{b}(\underline{f})$ , and integrate the “ordinary differential equation” (18) by a scheme to integrate ordinary differential equations, in our case a fourth order Runge-Kutta scheme:

$$\underline{f}_{i,j,k}^{l+1} = \underline{f}_{i,j,k}^l + \frac{1}{6} \left( \underline{k}_{i,j,k}^l + 2\underline{k}_{i,j,k}^{l+1/4} + 2\underline{k}_{i,j,k}^{l+1/2} + \underline{k}_{i,j,k}^{l+3/4} \right), \quad (19)$$

where

$$\begin{aligned} \underline{k}_{i,j,k}^l &= \Delta t \underline{B}(\underline{f}_{i,j,k}^l, \partial_i \underline{f}_{i,j,k}^l) \\ \underline{k}_{i,j,k}^{l+1/4} &= \Delta t \underline{B}(\underline{f}_{i,j,k}^{l+1/4}, \partial_i \underline{f}_{i,j,k}^{l+1/4}), \quad \underline{f}_{i,j,k}^{l+1/4} = \underline{f}_{i,j,k}^l + \frac{1}{2} \underline{k}_{i,j,k}^l \\ \underline{k}_{i,j,k}^{l+1/2} &= \Delta t \underline{B}(\underline{f}_{i,j,k}^{l+1/2}, \partial_i \underline{f}_{i,j,k}^{l+1/2}), \quad \underline{f}_{i,j,k}^{l+1/2} = \underline{f}_{i,j,k}^l + \frac{1}{2} \underline{k}_{i,j,k}^{l+1/4} \\ \underline{k}_{i,j,k}^{l+3/4} &= \Delta t \underline{B}(\underline{f}_{i,j,k}^{l+3/4}, \partial_i \underline{f}_{i,j,k}^{l+3/4}), \quad \underline{f}_{i,j,k}^{l+3/4} = \underline{f}_{i,j,k}^l + \underline{k}_{i,j,k}^{l+1/2} \end{aligned}$$

To carry over the convergence order of the time integration we must calculate the space derivatives in the source term with appropriate stencils. Best results are obtained, especially if space gradients dominate the error, by pseudo-spectral methods [17], which are of infinite order in space. Nevertheless, we do not want to use pseudo-spectral methods, because we want to keep the freedom to continue the calculation after singular values appeared at some gridpoints on a slice.

Instead of using spectral decompositions to calculate the space derivatives, we approximate derivatives by the symmetric fourth order stencil (10a), which stretches out two gridpoints to each side. To ensure stability we can, and actually we have to, add dissipative terms of higher order. For systems with constant coefficients theorem 6.7.1 and theorem 6.7.2 of [18] show stability. It is also discussed there how to extend results for systems with constant coefficients to systems with variable coefficients.

The dissipation term suggested by the theorems is

$$\begin{aligned} \partial_x^6 \underline{f}_{i,j,k}^l &= \frac{1}{(\Delta x)^6} \left( \underline{f}_{i-3,j,k}^l - 6\underline{f}_{i-2,j,k}^l + 15\underline{f}_{i-1,j,k}^l \right. \\ &\quad \left. - 20\underline{f}_{i,j,k}^l + 15\underline{f}_{i+1,j,k}^l - 6\underline{f}_{i+2,j,k}^l + \underline{f}_{i+3,j,k}^l \right), \end{aligned} \quad (20)$$

which has a seven point stencil stretching out three gridpoints on each side. By adding  $\sigma Q_2 := \frac{\sigma}{64N} (\Delta x)^5 \sum_{i=1}^N \partial_i^6 f$  with a sufficiently large  $\sigma$  to each evaluation of  $\underline{B}(\underline{f}, \partial_i \underline{f})$  we got a stable scheme. Numerical experiments showed that large values for  $\sigma$  require small time

steps  $\Delta t$  for stability, therefore  $\sigma$  should be chosen large enough, but as small as possible. The test cases have been run with  $\sigma = 2$ , other data may require larger values.

We also looked at a scheme which adds dissipation from a five point stencil after each full fourth order Runge-Kutta step, namely the term  $\sigma \bar{Q}_2 = \frac{-\sigma}{16N}(\Delta x)^4 \sum_{i=1}^N \partial_i^4 f$  with

$$\partial_x^4 \underline{f}_{i,j,k}^l = \frac{1}{(\Delta x)^4} \left( \underline{f}_{i-2,j,k}^l - 4\underline{f}_{i-1,j,k}^l + 6\underline{f}_{i,j,k}^l - 4\underline{f}_{i+1,j,k}^l + \underline{f}_{i+2,j,k}^l \right). \quad (21)$$

For  $\sigma = 2$  this also seems to be stable but it only yields a third order scheme and was therefore not pursued any farther.

In the numerical implementation we use four grids to store the variables, the gauge source functions, and the intermediate values. And again, even if we calculated the gauge source functions by some global fourth order procedure, the scheme would stay fourth order.

### C. The boundary treatment

There are two kind of boundaries to be dealt with. The first kind, which we call false boundaries, comes from reducing the grid size, but not the grid dimension, by assuming discrete symmetries. In our case these are the periodic boundaries in the  $y$  and  $z$  directions in asymptotically A3 spacetimes and the boundaries coinciding with the symmetry planes in octant<sup>4</sup> mode. On the false boundaries  $\Omega$  may assume any value. The second kind of boundaries, which we call true boundaries, restrict the treated range of the conformal spacetime. To avoid any significant influence of their treatment onto the physical spacetime they must be placed into regions with  $\Omega < 0$ .

In the first part of this series we have described how we change the equations near the true boundaries. For the tests we used the modification (I/19), which freezes the time evolution near the true boundaries.

Before we take a time step, we extend the grid on the true boundaries by the stencil width by a first order extrapolation. At false boundaries we extend by copying the values from the corresponding gridpoints in the interior. Then we take the time step and, of course, loose the just created gridpoints again.

### D. Controlling the time step

It is well-known that the Courant-Friedrichs-Lewy condition, which states that the numerical domain of dependence must contain the analytic domain of dependence, is necessary for stability of symmetric hyperbolic schemes. This requirement restricts the maximal size of the time step. To calculate a linear approximation to its size we take the forward light cone at all gridpoints  $(i, j, k)$  and calculate the time  $\Delta t_{\min i,j,k}$  of its earliest intersection with the boundaries given by the neighbouring gridpoints with coordinate values  $x_{i-1}$ ,  $x_{i+1}$ ,  $y_{j-1}$ ,

---

<sup>4</sup>Octant mode is obtained when assuming a mirroring symmetry with respect to the  $x$ ,  $y$ , and  $z$  plane through the origin.

$y_{j+1}$ ,  $z_{k-1}$ , and  $z_{k-1}$ . The minimum over the grid  $\Delta t_{\min} := \min_{(i,j,k)} \Delta t_{\min i,j,k}$  would be the maximally allowed time step for the pure rotated Richtmyer scheme. Stability requirements not caused by the CFL-condition and the use of wider stencils modify the allowed time step to a multiply  $q$  of  $\Delta t_{\min}$ . We ran all calculations reported in this paper with the value  $q = 1/2$ .

The time step control by linearly approximating the light cone has consequences for what we can expect, when we check convergence of a scheme by subtracting the results from runs with different coarseness of the grids at corresponding time steps. Since the size of the time steps deviates by second order, corresponding slices have time coordinates which deviate by second order. The sequence of the differences will therefore seem only second order convergent, even if the scheme really converges with higher order.

## IV. THE TESTS PERFORMED

### A. The exact solutions used for testing

To test the code we reproduce exact solutions of the conformal field equations by prescribing the data and the gauge source functions from the exact solutions. To better understand the test runs we shortly recall those properties of the used exact solutions which are important for us.

The first class of exact solutions, which we use in the 2D and 3D test runs, are the so-called asymptotically A3 solutions [19]. They are given by

$$\begin{pmatrix} g_{ab} \\ \Omega \end{pmatrix} = \begin{pmatrix} 4 \sqrt{\frac{2}{t_s^2 + x_s^2}} e^M (-dt_s^2 + dx_s^2) + \frac{1}{2} (t_s^2 + x_s^2) (e^W dy_s^2 + e^{-W} dz_s^2) \\ \frac{1}{4} (t_s^2 - x_s^2) \end{pmatrix}, \quad (22)$$

where  $M$  and  $W$  are certain functions of  $t_s$  and  $x_s$ .

If we set

$$(M, W) = (0, 0), \quad (23)$$

we obtain the A3 solution.

The choice

$$(M, W) = \left( -\frac{(t_s^2 + x_s^2)^2}{256}, \frac{t_s^2 - x_s^2}{8} \right) \quad (24)$$

yields a solution, which contains gravitational radiation [20]. Figure 3 shows a conformal diagram of asymptotically A3 solutions with the periodic  $y$  and  $z$  coordinates suppressed.

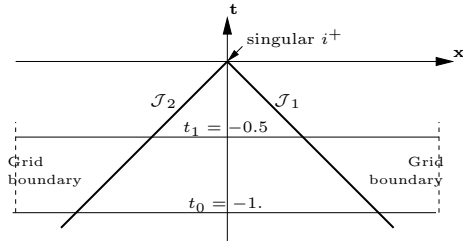


FIG. 3. Conformal spacetime for the asymptotically A3 spacetimes with  $y$  and  $z$  coordinate suppressed

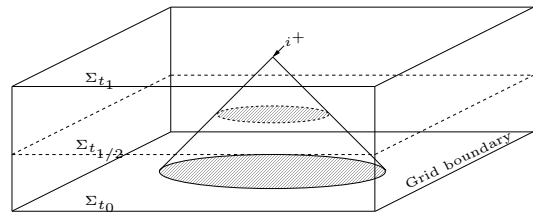


FIG. 4. Conformal Minkowski spacetime with  $z$  coordinate suppressed

We start at  $t_0 = -1$  and integrate until  $t_1 = -1/2$ . As long as  $t_0$  and  $t_1$  are negative, their choice is completely arbitrary. The origin  $(0,0)$  is singular, the components of the metric and the curvature become singular there. In principle we could continue the calculation beyond  $t_1$  towards  $(t_s, x_s) = (0,0)$ , and for test purposes we have done so. The CFL condition then forces us to use smaller and smaller time steps and we approach, but never reach, the origin.

In the calculations reported here we have hidden the symmetries in the 2D calculations by the transformation

$$\begin{pmatrix} t_s \\ x_s \\ y_s \end{pmatrix} = \begin{pmatrix} t \\ x \left\{ 1 + \frac{1}{2} (x-1) \left[ \sin \left( \pi \frac{y-y_{\min}}{y_{\max}-y_{\min}} \right) \right]^2 \right\} \\ y \end{pmatrix} \quad (25)$$

and in the 3D calculations by the transformation

$$\begin{pmatrix} t_s \\ x_s \\ y_s \\ z_s \end{pmatrix} = \begin{pmatrix} t \\ x \left\{ 1 + \frac{1}{2} (x-1) \left[ \sin \left( \pi \frac{y-y_{\min}}{y_{\max}-y_{\min}} \right) \right]^2 \left[ \sin \left( \pi \frac{z-z_{\min}}{z_{\max}-z_{\min}} \right) \right]^2 \right\} \\ y \\ z \end{pmatrix}. \quad (26)$$

Another exact solution, we have tested against, is the conformal representation of Minkowski spacetime, which is in spherical coordinates  $(t, r, \theta, \varphi)$  given by

$$\begin{pmatrix} g_{ab} \\ \Omega \end{pmatrix} = \begin{pmatrix} -dt^2 + dr^2 + (\sin r)^2 [d\theta^2 + (\sin \theta)^2 d\varphi^2] \\ 2 / \sqrt{\left(1 + \left(\tan \frac{t+r}{2}\right)^2\right) \left(1 + \left(\tan \frac{t-r}{2}\right)^2\right)} \end{pmatrix}. \quad (27)$$

Of course, in the actual calculation we have transformed to Cartesian coordinates, where  $g_{ab}$  is no longer diagonal and the spherical symmetry is hidden. It should also be mentioned that this conformal solution is time dependent, since the conformal factor  $\Omega$  is. But the time dependence is in a certain sense very weak, already the test calculations for the spherically symmetric case in [21] have shown, that the accuracy obtained is order of magnitudes better than what is obtained in interesting cases. This statement is confirmed by the results of subsection IV D.

Due to our boundary treatment we can expect the reproduction of the exact solution and the propagation of the constraints only at gridpoints representing physical spacetime and  $\mathcal{J}$ , although the solutions given exist outside the physical region. Therefore, we apply the measures for the quality of a solution, as defined in subsection IV B, only at the gridpoints representing physical spacetime. In the used representation of conformal Minkowski spacetime we reach timelike infinity  $i^+$  after a finite conformal time. Hence, the number of gridpoints representing physical spacetime decreases to zero. To have a significant part of the grid available to evaluate our accuracy measures we compare on the slice half way to  $i^+$ , although the calculations have been continued beyond  $i^+$ . Even when surpassing  $i^+$  there is no change in the convergence of the scheme. By being able to cover timelike infinity with gridpoints we have a powerful numerical tool to study the fall-off behaviour of radiative

quantities for very long times [10].

Another solution which is commonly used for testing codes in numerical relativity is the Schwarzschild solution. So, why is this code not yet tested against the Schwarzschild solution? The reason is simple: The author is not aware of any explicit solutions of the conformal field equations representing the Schwarzschild-Kruskal spacetime, which is regular at both  $\mathcal{S}$ s and which is smoothly extendible across both  $\mathcal{S}$ s. By Birkhoff's theorem, the theorems in [3], and the theorems in [2] we know that all the requirements above can be achieved, except that the solution is not explicit. When describing the initial data solver part of the code, we are going to prescribe spherically symmetric free functions with two  $\mathcal{S}$ s, which then necessarily yield data for the Schwarzschild-Kruskal spacetime.

## B. Measures for the quality of a numerical solution

Without doubt, the best measure for the quality of a numerical solution is the difference to the exact solution:

$$\Delta_{i,j,k} := \underline{f}_{i,j,k} - \underline{f}_{\text{exact } i,j,k}, \quad (28)$$

where  $\{i, j, k\}$  denotes gridpoints representing physical spacetime or null infinity. Since gravitational radiation is given by the Newman-Penrose quantity  $\psi_4$  of the conformal Weyl tensor  $d_{abc}{}^d$  evaluated at  $\mathcal{J}$ , which is essentially a polynomial expression in  $E_{ab}$  and  $B_{ab}$ , the error in  $E_{ab}$  and  $B_{ab}$  is also a measure for the error in the gravitational radiation. As we do not prescribe all variables when providing an exact solution, but numerically calculate  ${}^{(1,1)}\hat{R}_{ab}$ ,  $E_{ab}$ , and  $B_{ab}$  by solving elliptic equations, the comparison of all variables with the exact solution is very time consuming, especially since the AMG library does not run in parallel. We therefore compare with the exact solution only once towards the end of a calculation. On the intermediate time steps we use what we call pseudo-difference, that is we calculate  $(h_{ab}, k_{ab}, \gamma^a{}_{bc}, {}^{(0,1)}\hat{R}_a, f_{(1,1)\hat{R}ab}, \Omega f_{Eab}, f_{Bab}, \Omega, \Omega_0, \Omega_a, \omega)$  from the exact solution given by  $(g_{ab}, \Omega)$  and compare with  $(h_{ab}, k_{ab}, \gamma^a{}_{bc}, {}^{(0,1)}\hat{R}_a, \Omega {}^{(1,1)}\hat{R}_{ab}, \Omega^2 E_{ab}, \Omega B_{ab}, \Omega, \Omega_0, \Omega_a, \omega)$ . Comparisons of the measure “difference” and “pseudo-difference” have been performed and the comparisons showed that the measures are measures exchangeable with respect to the relative error, which we define as

$$\Delta_{\text{rel } i,j,k} := \frac{\underline{f}_{i,j,k} - \underline{f}_{\text{exact } i,j,k}}{\max_{(i,j,k)}(1, |\underline{f}_{i,j,k}|)}. \quad (29)$$

With respect to the absolute error the results differ, since e. g.  $\Omega^2 E_{ab}$ , which is used in pseudo-difference, may be significantly smaller than  $E_{ab}$ , and since the variables representing second derivatives of the metric, like  $E_{ab}$ , tend to dominate the absolute error.

We also monitor the violation of the constraints. In later runs, which do not reproduce an exact solution, the convergence of the violation of the constraints to zero is our main criteria for consistency of the numerical time evolution with the Einstein equation, although we cannot conclude from the size of the numerical constraint violation to the quality of the numerical solution [22].

When debugging and analysing the performance of the code we look at the measures point-wise by looking at surface plots on well-chosen two-dimensional slices. Although this implies looking at hundreds of plots to get representative samples, we regard it as unavoidable for a thorough testing and tuning of the code. Since we cannot present hundreds of figures in a paper we must condense for the presentation in this paper. To do so, we plot

$$\|\Delta\|(x) := \frac{1}{M} \sqrt{\sum_{l=1}^M \int_{\{y,z\}} (\Delta_l(x, y, z))^2 dy dz} \sim \frac{1}{M} \sqrt{\frac{1}{N_y N_z} \sum_{l=1}^M \sum_{\{j,k\}} (\Delta_{l,j,k})^2}, \quad (30)$$

where  $M$  is the number of the entries in the vector  $\underline{\Delta} = \Delta_l$  of quantities which should go to zero.

### C. Tests of the 2D code

In the first tests we ran we did not hide the obvious Killing vector  $\partial_{y_s}$  in expression (22). The only remarkable thing to report about is, that in this case we could find a stable treatment of the true boundaries without changing the equations near the true boundaries as described in subsection III C. For solutions with hidden Killing vectors the first became unstable, forcing us to introduce the later treatment.

From the numerical viewpoint, solution (23), the A3 solution without gravitational radiation, and solution (24), a solution with gravitational radiation, behave very similar.

Figure 5 shows the convergence of the second order scheme in the measure (30), where  $\Delta_l$  denotes the pseudo-difference to the exact solution at  $t_1 = -1/2$ .

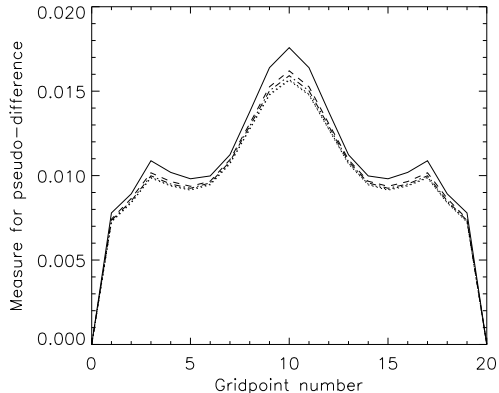


FIG. 5. Convergence against an A3 like solution for the 2nd order scheme in 2D

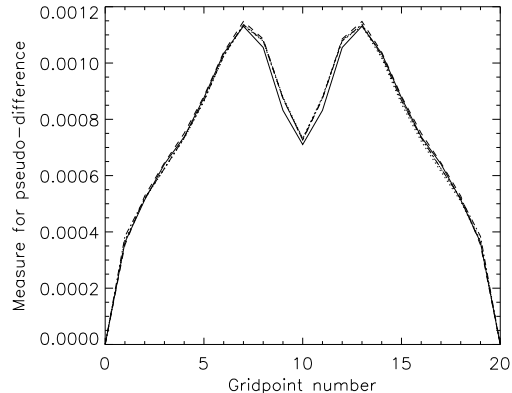


FIG. 6. Convergence against an A3 like solution for the 4th order scheme in 2D

The lines plotted correspond to calculations with  $40^2$  (solid),  $80^2$  (dashed),  $160^2$  (dotted),  $320^2$  (dash-dot), and  $640^2$  gridpoints (dotted). The values are scaled in such a way that the lines would coincide, if the convergence were exactly second order. The gridpoint numbers are with respect to the output grid which has a constant number of gridpoints independent of the grid on which the calculation is performed. Obviously in the calculation with  $40^2$  gridpoints higher order terms still make a significant contribution to the error, the solid

line does not coincide with the dashed line. For finer grids we get the expected rate of convergence.

Since the size of the error measure is not immediately related to the maximum norm of the error, we give it as well: The maximum of the absolute error drops in good agreement with the convergence rate from 4.44 in the  $40^2$  run to 0.01 in the  $640^2$  run. The variable with the largest error is in both cases  $E_{11}$ . The variable with the largest relative error is  $k_{11}$ , its value drops, again in good agreement with the convergence rate, from 17% to 0.07%.

Figure 7 shows the scaled measures for the violation of the constraints.

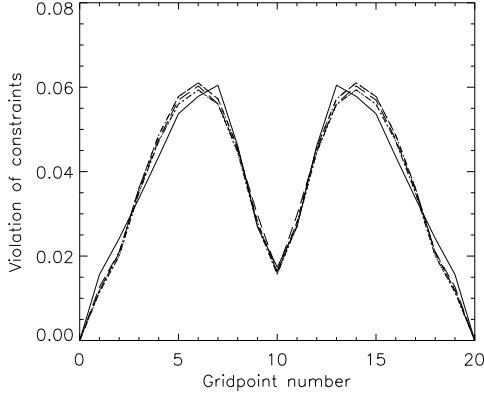


FIG. 7. Convergence of the violation of the constraints in an A3 like solution for the 2nd order scheme in 2D

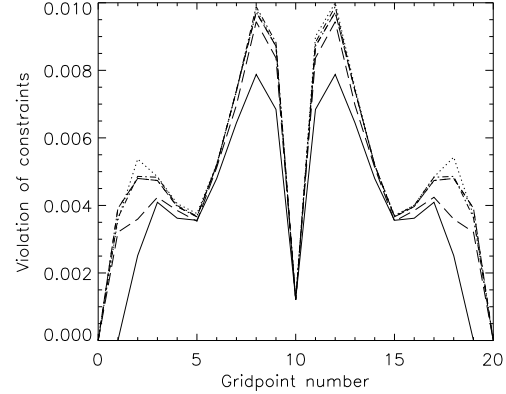


FIG. 8. Convergence of the violation of the constraints in an A3 like solution for the 4th order scheme in 2D

Since all the curves almost coincide, the violation of the constraints converges to zero in excellent agreement with the convergence order.

Figure 6 is the analogue to figure 5 for the fourth order scheme, but with a fourth order scaling. We observe that already for the  $40^2$  run the error is dominated by fourth order contributions. Already for this coarsest grid, the error measure is one order of magnitude smaller than what we obtained for the second order scheme. This result is also confirmed by the figures for the maximum norm, which are: The maximal absolute error drops from 1.35 to  $2.1 \times 10^{-5}$  and is found as in the second order scheme in the variable  $E_{11}$ . In contrast to the second order scheme, the maximal relative error appears for the variable  $E_{12}$  and decreases from 6.2% to  $1.0 \times 10^{-4}\%$ . This is all in excellent agreement with fourth order convergence.

Good, but not excellent agreement with fourth order convergence can be found in figure 8, which shows the convergence of the violation of the constraints. The scaled curves for the  $40^2$  (solid line) and the  $80^2$  (dashed line) deviate from the curves for runs with finer grids ( $160^2$  and  $320^2$ ), which coincide very well. The dashed-dotted line representing the  $640^2$  run deviates slightly around gridpoint 2 and 18 from the  $160^2$  and the  $320^2$  runs. This is not serious, in this run we have reached the lower accuracy bound at which rounding errors inherited from the “ $\Omega$  divider” become significant (see also the discussion at the end of subsection II C).



## D. For 3D

### 1. Minkowski

Figure 9 and figure 10 show the measure for the pseudo-difference for a second and a fourth order 3D run with  $50^3$  (solid line) and  $100^3$  (dashed line) with data for the Minkowski spacetime.

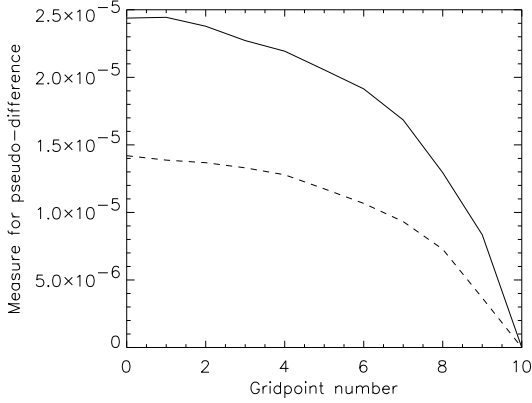


FIG. 9. Convergence against the Minkowski solution for the 2nd order scheme in 3D

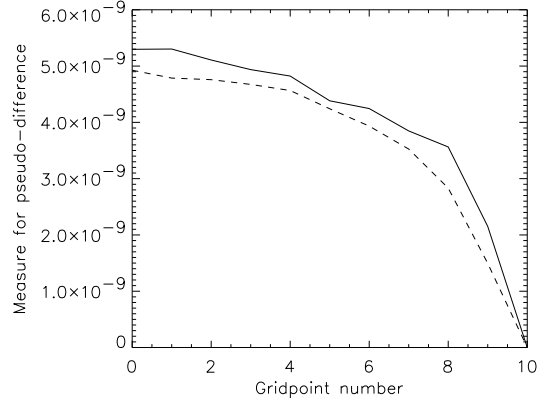


FIG. 10. Convergence against the Minkowski solution for the 4th order scheme in 3D

The solid line is scaled such that with exact convergence it would lie on the dashed line. Although the runs have been done on a full grid, despite the octant symmetry, the figures are based on an octant. We immediately see, that, due to the low number of gridpoints, the error of both schemes has contributions from higher order terms. These higher order contributions are more significant in the second order run. We do not regard this failure as very serious as the achieved accuracy is already extremely high.

In the  $100^3$  run the maximum of the absolute error is extremely small, it is  $6.6 \times 10^{-5}$  for  ${}^{(1,1)}\hat{R}_{33}$  in the second order run and  $2.2 \times 10^{-8}$  for  ${}^{(1,1)}\hat{R}_{33}$  in the fourth order run. The exactly same numbers hold for what we have defined as the maximal relative error.

If we calculate under the assumption of second order convergence, what grid size we would need to achieve in a second order run the same accuracy with respect to the maximum of the relative error as in the  $100^3$  fourth order run, we get a hypothetical  $5400^3$  grid. Due to the already very small error in both schemes we regard that estimate as meaningless for practical purposes.

### 2. A3

Figure 11 and figure 12 show the measure for the pseudo-difference for a second and a fourth order 3D run with  $50^3$  (solid line) and  $100^3$  (dashed line) on an A3 like spacetime with hidden  $y$  and  $z$  Killing symmetries.

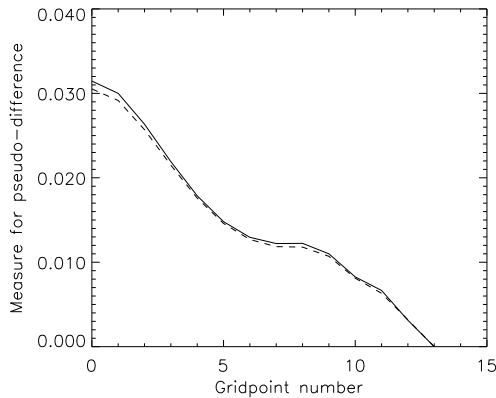


FIG. 11. Convergence against an A3 like solution for the 2nd order scheme in 3D

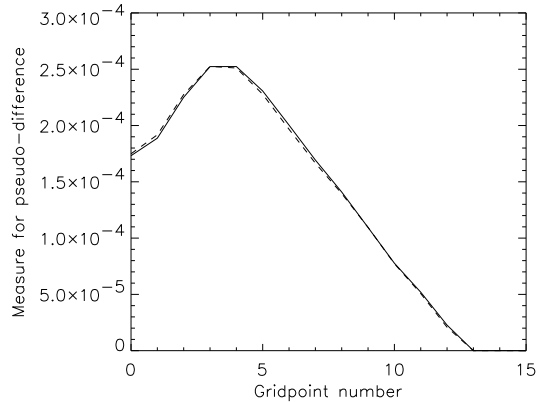


FIG. 12. Convergence against an A3 like solution for the 4th order scheme in 3D

Again the solid line is scaled such that with exact convergence it would lie on the dashed line and we only plot an octant. The order of convergence is in excellent agreement with the prediction, the contribution of higher order terms to the error is almost negligible.

With the  $100^3$  grid the maximum of the absolute error is 0.41 for  $E_{11}$  in the second order run and 0.077 for  $E_{11}$  in the fourth order run. The largest relative error is 5.8% for  $B_{11}$  in the second order run and 0.24% for  $E_{23}$  in the fourth order run.

If we again calculate under the assumption of second order convergence, what grid size we would need to achieve in a second order run the same accuracy with respect to the maximum of the relative error as in the  $100^3$  fourth order run, we get a hypothetical  $490^3$  grid. With respect to the  $L_2$ -Norm of the pseudo-difference we would even need  $1000^3$  gridpoints.

## V. CONCLUSION

In this paper we have described a method and its numerical implementation to derive a complete set of data for the conformal field equations from a minimal set which works for all scenarios described in subsection III/B of [1].

Using data derived from a minimal set given by exact solutions we have tested our time integration code and compared a second with a fourth order scheme. This comparison turned out to be disastrous for the second order scheme. To reproduce the accuracy of a maximal relative error smaller than one percent in a situation with gravitational radiation, as achieved by a  $100^3$  grid in the fourth order run, which needs 1.7 GB of memory and 7 hours on 16 processors of a origin 2000, we would need more than 200 GB memory and 3000 hours on 16 processors for a run with the second order scheme.

## ACKNOWLEDGEMENT

I would like to thank B. Schmidt and J. Frauendiener for many fruitful discussions. In particular I would like to thank H. Friedrich for his extensive help and support.

On numerical questions I got indispensable help from H.-O. Kreiss, who pointed out to me the superiority of the methods of line, and K. Stüben from the Gesellschaft für Mathematik

und Datenverarbeitung, who put the Algebraic Multigrid Library at my disposal and was very helpful whenever I had “elliptic problems”.

## APPENDIX A: REMARKS ABOUT THE COMPUTATIONAL SCIENCE ASPECT OF THE CODE

We now give a short review of the computational science aspect of the code.

To be able to do calculations of spacetimes with low symmetries, especially 3D calculations, it is highly recommendable to do the resource intensive parts of the calculations in parallel. On the other side, development of parallel program code tends to take much longer than writing serial code. It is therefore advantageous to be able to execute serial as well as parallel sections in one program, one then has the freedom to program less resource intensive tasks serial and to save human resources. The most used library for parallel computing, MPI, does not allow to combine parallel and serial code, since the library does not require the processors to share a common address space for their memory. We therefore decided to require shared memory, a modern hardware technology, which provides a common address space, and to use POSIX threads to achieve parallelism.

In 2D and 3D time evolutions of the conformal field equations the code scales very well and on a 27 processor<sup>5</sup> run we typically get a speed-up of 24. The remaining gap is mostly due to the variable work load per gridpoint caused by the change of the equations near the boundary as described in equation (I/19). For systems with a constant work load per gridpoint, e. g. 3D Maxwell equations on periodic grids, we come significantly closer to the optimal speed-up of 27.

With the exception of dumping intermediate results to checkpoint, all output of data is done in the XDR format to generate hardware independent binaries. The output interface allows the caller to request and get the output of arbitrary rectangular sections of the grid with arbitrary coarseness for each coordinate.

The interaction between the parts of the code which provide the computational infrastructure and the parts which are equation or boundary specific has been minimised. The code was successfully used to numerically solve initial value problems for the 3D Maxwell equations on periodic grids, the 3D SU(2) Yang-Mills equations on periodic grids, and the 1D, 2D, and 3D conformal field equations for boundaries periodic in y and z direction, for normal boundaries in all directions, and for octant mode.

In [23] we describe why we believe that a numerical relativity code should be able to deal with variables becoming singular at gridpoints. Since we want to also implement a similar strategy in more than 1D later, the code is designed to allow a future extension to include handling and bookkeeping of singular gridpoints. Since the implementation of this extension was not necessary for the purposes of this paper, it is due. Its description will be the last part of this series.

---

<sup>5</sup>The maximal number of processors available for a single user on our computer.

- [1] P. Hübner, gr-qc **9804**, 1 (1998).
- [2] H. Friedrich, J. Differential Geometry **34**, 275 (1991).
- [3] L. Andersson, P. T. Chrusciel, and H. Friedrich, Comm. Math. Phys. **149**, 587 (1992).
- [4] J. Frauendiener, gr-qc **9806**, 1 (1998).
- [5] K. Stüben, private communication.
- [6] W. Hackbusch, in *Theorie und Numerik elliptischer Differentialgleichungen*, edited by (Teubner, Stuttgart, 1996).
- [7] K. Stüben, GMD report (1999).
- [8] J. W. Ruge and K. Stüben, in *Multigrid Methods*, SIAM, edited by S. F. McCormick (Society for Industrial and Applied Mathematics, Philadelphia, 1987), pp. 73–130.
- [9] R. W. Corkill and J. M. Stewart, Proc. R. Soc. Lond. A **386**, 373 (1983).
- [10] P. Hübner, Helv Phys Acta **69**, 316 (1996).
- [11] R. Peyret and T. D. Taylor, *Computational Methods for Fluid Flow*, Springer Series in Computational Physics (Springer-Verlag New York, 1983).
- [12] E. Turkel, Journal of Computational Physics **15**, 226 (1974).
- [13] R. D. Richtmyer and K. W. Morton, in *Difference Methods for Initial-value Problems*, edited by L. Bers, R. Courant, and J. J. Stoer (Interscience Publishers, New York, 1967).
- [14] G. Engeln-Müllges and F. Reutter, in *Formelsammlung zur Numerischen Mathematik mit Standard-FORTRAN-Programmen* (B.I.-Wissenschaftsverlag, 1984).
- [15] J. C. Wilson, J. Inst. Maths Applies **10**, 238 (1972).
- [16] H.-O. Kreiss, private communication.
- [17] B. Fornberg, in *A Practical Guide to Pseudospectral Methods*, edited by P. G. Ciarlet, A. Iserles, R. V. Kohn, and M. H. Wright (Cambridge University Press, Cambridge, 1996).
- [18] B. Gustafsson, H.-O. Kreiss, and J. Olinger, in *Time Dependant Problems and Difference Methods*, Pure and Applied Mathematics, edited by M. B. Allen *et al.* (John Wiley & Sons, Inc., New York, 1995).
- [19] P. Hübner, Class. Quantum Grav. **15**, L21 (1998).
- [20] T. Foertsch, Master’s thesis, Techn. Universität Berlin, 1997.
- [21] P. Hübner, Ph.D. thesis, Ludwig-Maximilians-Universität München, 1993.
- [22] M. W. Choptuik, Phys. Rev. D **44**, 3124 (1991).
- [23] P. Hübner, Phys. Rev. D **53**, 701 (1996).